Application of STAP in Advanced Sensor Systems

William L. Melvin
Georgia Tech Research Institute
7220 Richardson Road
Smyrna, GA 30080, USA

bill.melvin@gtri.gatech.edu

Summary

Space-time adaptive processing (STAP) is a multidimensional analog of the well-known, one-dimensional adaptive sidelobe canceler developed in the late 1950's. It enables adaptive cancellation of interference in a two-dimensional space. When the two-dimensional target power spectral density differs from that of the interference, STAP leads to enormous improvements in target detection potential. Owing to this potential, STAP has application to current and future airborne, spaceborne, bistatic and ground-based radar sensors; in this set of lecture notes, we consider the role STAP plays in each of these systems. We begin with the airborne case, describing the nature of ground clutter and its impact on target detection. This serves as segue to a discussion of STAP and its comparison with competing methods. Next, we consider spaceborne radar systems. Since STAP is a member of the class of super-resolution algorithms, it enables the design of spaceborne moving target indication radar with smaller aperture; this is an important consideration when launching the satellite radar system. Bistatic systems must contend with spectrally severe ground clutter returns, for which STAP offers a potential solution. Herein, we describe bistatic STAP, with particular emphasis on the nonstationary nature of the bistatic clutter environment. We conclude by considering STAP application to terrain scattered jamming; ground based radar serves as the focus of this final discussion.

1. Introduction

In [1], we discuss the basic theory of space-time adaptive processing (STAP) and related detection theory. This set of lecture notes considers practical aspects of STAP. Moving target indication (MTI) serves as our primary focus.

STAP is a higher dimensional version of the adaptive sidelobe canceler developed in the late 1950's and early 1960's [2]. Reed and Brennan discuss the theory of STAP for airborne radar in a seminal 1973 paper [3]. In years since the Brennan and Reed paper, STAP has been vigorously researched. The recent advancement of high speed, high performance digital signal processors now make fielding STAP-based radar systems a reality. We consider the use of STAP in diverse aerospace radar applications in this paper, examining airborne, spaceborne and bistatic systems. Additionally, we describe STAP for terrain scattered jamming (TSJ) mitigation.

Radar sensors can measure spatial direction of arrival in azimuth and elevation, or cone angle; slow-time phase progression; fast-time delay; and, polarization. Additionally, the processor can operate on data taken over multiple radar scans. Adaptive processing exploits this signal diversity to enhance detection capability. The Fourier transforms of slow-time and fast-time yield Doppler frequency and range information, respectively. By subarraying an electronically scanned antenna (ESA) into multiple receive channels, the radar can measure direction of arrival. A linear antenna measures cone angle [4], an ambiguous measurement resulting from the linear array's inability to separate time delay attributable to either azimuth or elevation angles.

Aerospace radar must cope with ground clutter while attempting to detect airbreathing or surface moving targets. The platform velocity induces a clutter Doppler shift varying over angle. Thus, ground clutter exhibits coupling in both angle and Doppler. The locus of points in the angle-Doppler power spectral density

Paper presented at the RTO SET Lecture Series on "Military Application of Space-Time Adaptive Processing", held in Istanbul, Turkey, 16-17 September 2002; Wachtberg, Germany, 19-20 September 2002; Moscow, Russia, 23-24 September 2002, and published in RTO-EN-027.

(PSD) corresponding to ground clutter signals is known as the clutter ridge [4-5]. STAP provides a means of suppressing clutter by exploiting spatial and temporal signal diversity. In this case, slow-time measurements provide the necessary temporal degrees of freedom (DoF).

Since narrowband jamming is correlated in angle, spatial diversity (adaptive notching in azimuth or elevation sidelobes) adequately suppresses the jamming signal. Mainlobe jammer mitigation is much more challenging. Terrain scattered jamming (TSJ) – jamming energy scattered of the earth's surface – enters the mainlobe of the antenna. For this reason, spatial diversity by itself does not provide adequate jammer suppression. Since the jammer does not exhibit correlation over slow-time, diversity in this domain is of no value. However, the jammer waveform exhibits correlation in the fast-time dimension. Hence, the digital signal processor can adaptively combine spatial and fast-time measurements to cancel TSJ while passing the target signal with maximal gain. This adaptive processing scheme is also referred to as STAP; fast-time signal diversity, versus slow-time, is implied.

In Section 2 we discuss fundamental aspects of ground clutter mitigation for the airborne radar platform. We define the airborne MTI and ground MTI missions and identify advantages STAP offers for these particular applications. Furthermore, we develop models for ground clutter and narrowband noise jamming. We delve into important aspects of the null-hypothesis covariance matrix and examine adaptive training issues. We include measured radar data examples.

Section 3 builds on results from Section 2, describing STAP for spaceborne radar systems. We investigate the key distinctions between airborne and spaceborne radar systems, examine STAP's role in overcoming aperture limitations, and provide simulated data examples showing the behavior of ground clutter in a notional space-based radar (SBR). Section 4 develops a basic understanding of the issues in bistatic STAP. Clutter nonstationarity is the key consideration in the bistatic case. Using numerical simulation, we examine STAP performance applied to multichannel bistatic radar data. We conclude by examining TSJ suppression using STAP in Section 5. We develop basic jammer space and fast-time models and a space-(fast)time adaptive processing implementation.

In the following discussion, the term *interference* subsumes both clutter and noise jamming signals. Signal-to-interference-plus-noise-ratio (SINR) describes the output signal power relative to the interference. Signal-to-noise ratio (SNR) is characteristic of output signal power relative to uncorrelated system noise, and thus characterizes the noise-limited performance of the radar.

2. STAP in Airborne Radar

Moving target indication (MTI) radar must detect, track and identify targets of various classes. Adequate target detection is fundamental to all other processing steps. The target Doppler shift often helps distinguish a mover from stationary ground clutter. However, in many cases, Doppler processing alone does not adequately enhance SINR, and so missed detections result. By adapting over space and slow-time samples, STAP increases SINR, consequently improving detection performance.

Two classes of MTI radar exist. Airborne moving target indication (AMTI) involves the detection of airbreathing vehicles. Such targets generally have relatively high radial velocities and lower radar cross sections. The maneuverability of the target limits the coherent dwell, hence lessening the attainable integration gain and Doppler resolution. Sidelobe clutter is a major impediment in AMTI. On the other hand, ground moving target indication (GMTI) involves detecting slower moving surface targets. Ground targets generally are less mobile and exhibit higher radar cross section than their airborne counterparts. The potential for longer dwell time suggests enhanced output SNR. However, the low radial velocity of the target places it in direct competition with strong mainbeam clutter. Figure 1 is a notional view of clutter, jamming and a moving target signal. Projecting into the angle domain, we find that mainbeam clutter masks the target; conversely, projecting into the Doppler domain, the problematic nature of sidelobe clutter and noise jamming is evident. STAP attempts to optimize a two-dimensional space-time filter response at a given range cell to maximize SINR.

A collection of many scatterers along an iso-range comprises the ground clutter return. An approximation to the corresponding clutter space-time snapshot for the k^{th} range is

$$\mathbf{x}_{k/C} = \sum_{m=1}^{N_c}\sum_{n=1}^{N_a} \boldsymbol{\alpha}_{m,n} \odot \mathbf{s}_{s\text{-}t}(\phi_{m,n}, \theta_{m,n}, f_{d/m,n}) \tag{1}$$

where N_c is the number of clutter patches, N_a is the number of range ambiguities, $\boldsymbol{\alpha}_{m,n} \in C^{NMx1}$ is the vector of voltages observed at each of M spatial channels over N pulses, and $\mathbf{s}_{s\text{-}t}(\phi_{m,n}, \theta_{m,n}, f_{d/m,n}) \in C^{NMx1}$ is the space-time steering vector for the m-n^{th} clutter patch. We denote azimuth as $\phi_{m,n}$, elevation as $\theta_{m,n}$ and Doppler frequency as $f_{d/m,n}$ for each clutter patch. Assuming statistical independence among clutter patches, the clutter covariance matrix is then given by

$$\begin{aligned}\mathbf{R}_{k/C} = E[\mathbf{x}_{k/C}\mathbf{x}_{k/C}^H] &= \sum_{m=1}^{N_c}\sum_{n=1}^{N_a} E\left[\left(\boldsymbol{\alpha}_{m,n} \odot \mathbf{s}_{s\text{-}t}(\phi_{m,n}, \theta_{m,n}, f_{d/m,n})\right)\left(\boldsymbol{\alpha}_{m,n} \odot \mathbf{s}_{s\text{-}t}(\phi_{m,n}, \theta_{m,n}, f_{d/m,n})\right)^H\right] \\ &= \sum_{m=1}^{N_c}\sum_{n=1}^{N_a} E\left[\boldsymbol{\alpha}_{m,n}\boldsymbol{\alpha}_{m,n}^H\right] \odot \mathbf{s}_{s\text{-}t}(\phi_{m,n}, \theta_{m,n}, f_{d/m,n})\mathbf{s}_{s\text{-}t}^H(\phi_{m,n}, \theta_{m,n}, f_{d/m,n}).\end{aligned} \tag{2}$$

The symbol $\odot$ denotes "element-wise" product. We also define $\mathbf{A}_c = \mathrm{E}\left[\boldsymbol{\alpha}_{m,n}\boldsymbol{\alpha}_{m,n}^{\mathrm{H}}\right]$ as the space-time correlation matrix. $\mathbf{A}_c$ simultaneously describes the statistical nature of voltage fluctuations from pulse-to-pulse and any spatial decorrelation due to non-zero bandwidth. If the voltage due to each target scatterer is constant over the dwell, and the bandwidth is sufficiently narrow (a fraction of a percent of the radar center frequency), then (2) becomes

$$\mathbf{R}_{k/C} = E[\mathbf{x}_{k/C}\mathbf{x}_{k/C}^H] = \sum_{m=1}^{N_c}\sum_{n=1}^{N_a} \sigma_{C/m,n}^2 \, \mathbf{s}_{s\text{-}t}(\phi_{m,n}, \theta_{m,n}, f_{d/m,n})\mathbf{s}_{s\text{-}t}^H(\phi_{m,n}, \theta_{m,n}, f_{d/m,n}), \tag{3}$$

where $\sigma_{C/m,n}^2$ is the single channel, single pulse clutter power for the m-n^{th} patch.

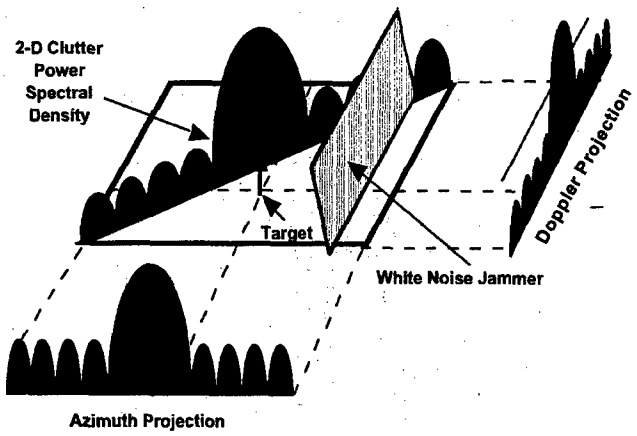

Figure 1. Notional view of the airborne radar detection problem. Clutter and jamming mask the target.

A model for the m^{th} narrowband jammer space-time snapshot is given by

$$\mathbf{x}_{k/J,m} = \sigma_{J/m}\left(\mathbf{u}_N \otimes \mathbf{s}_s(\phi_m, \theta_m)\right); \;\; \mathbf{u}_N \sim CN(\mathbf{0}, \mathbf{I}_N) \tag{4}$$

where $\sigma_{J/m}$ is the single channel jammer power. The complete jammer snapshot is $\mathbf{x}_{k/J} = \sum_{m=1}^{N_j} \mathbf{x}_{k/J,m}$ for N_j noise jamming sources. Since each jammer is uncorrelated and the jamming voltage is Gaussian, the jammer covariance matrix for the k^{th} range is expressible as

$$\begin{aligned} \mathbf{R}_{k/J} &= \sum_{m=1}^{N_j} \mathrm{E}\left[\mathbf{x}_{k/J,m}\mathbf{x}_{k/J,m}^{H}\right] = \sum_{m=1}^{N_j} \mathbf{R}_{k/J,m}; \\ \mathbf{R}_{k/J,m} &= \mathrm{E}\left[\mathbf{x}_{k/J,m}\mathbf{x}_{k/J,m}^{H}\right] = \sigma_{J/m}^{2}\left(\mathbf{I}_N \otimes \mathbf{s}_s(\phi_m', \theta_m)\mathbf{s}_s^{H}(\phi_m, \theta_m)\right), \end{aligned} \tag{5}$$

reflecting the fact that the jammer is spatially correlated (the $\mathbf{s}_s\mathbf{s}_s^H$ term in (5)), yet white in Doppler (the $\mathbf{I}_N$ term in (5)).

The ultimate limitation on detection performance is additive thermal noise generated by the radar receiver. Though an approximation, it is common to assume the receiver noise is white in space and time. Under such circumstances, the receiver noise covariance matrix for the noise snapshot $\mathbf{x}_{k/n}$ takes the form

$$\mathbf{R}_{k/n} = \sigma_n^2 \mathbf{I}_{NM}, \tag{6}$$

where σ_n^2 is the single channel noise variance.

The space-time snapshot is the additive combination of clutter, jamming and receiver noise snapshots. Each component is statistically independent. Thus, the space-time snapshot and covariance matrix are

$$\begin{aligned} \mathbf{x}_k &= \mathbf{x}_{k/C} + \mathbf{x}_{k/J} + \mathbf{x}_{k/n}; \;\; \mathbf{x}_k \sim \mathrm{CN}(\mathbf{0}, \mathbf{R}_k); \\ \mathbf{R}_k &= \mathbf{R}_{k/C} + \mathbf{R}_{k/J} + \mathbf{R}_{k/n}. \end{aligned} \tag{7}$$

The power spectral density (PSD) is the Fourier transform of the covariance matrix, $\mathbf{R}_k \overset{\mathfrak{I}}{\leftrightarrow} \mathrm{PSD}$, and is a typical approach for viewing those two-dimensional frequencies occupied by colored noise. Figure 2 is an example of a typical angle-Doppler PSD for a side-looking airborne radar system. Clutter and jamming are identified in the figure. Figure 3 shows a periodogram approximation to the PSD for actual measured airborne radar data taken from the Multichannel Airborne Radar Measurements (MCARM) program [6]; as one would expect, the clutter ridge is readily apparent in this figure.

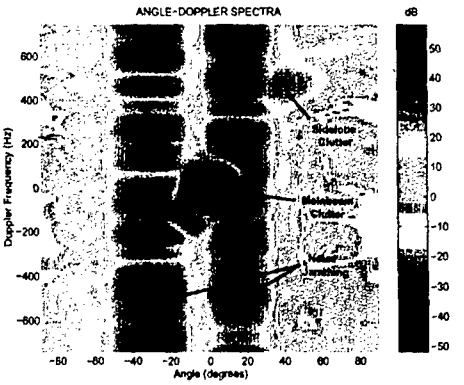

Figure 2. Angle-Doppler power spectral density, medium PRF, side-looking radar case.

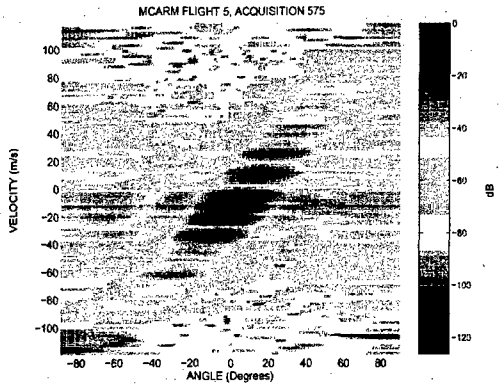

Figure 3. Clutter only power spectral density estimate for measured multi-channel airborne radar data collected as part of the Multi-Channel Airborne Radar Measurements (MCARM) effort.

An alternate spectral view is the minimum variance distortionless response (MVDR) spectra,

$$\mathrm{MVDR}(\phi_m,\theta_m,f_{d/m}) = \frac{1}{\mathbf{s}_{s\text{-}t}^{H}(\phi_m,\theta_m,f_{d/m})\mathbf{R}_k^{-1}\mathbf{s}_{s\text{-}t}(\phi_m,\theta_m,f_{d/m})}. \tag{8}$$

The MDVR spectra provides a super-resolution view of the interference. Figure 4 compares the MVDR spectra for the side-looking airborne radar example of Figure 2. In contrast, Figure 5 shows the MVDR spectra for the forward-looking radar case. The clutter ridge opens up into an ellipse for the forward-looking case; two stationary ground points on either side of the aircraft velocity vector possess the same Doppler but mirror symmetric direction of arrival.

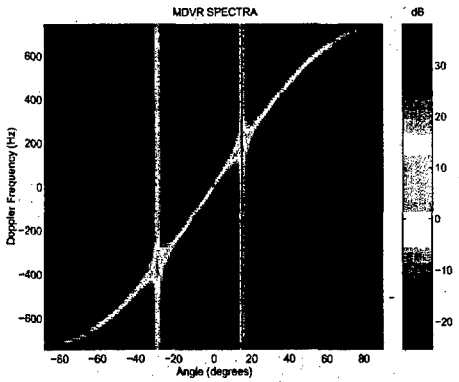

Figure 4. MVDR spectra, medium PRF, side-looking radar case.

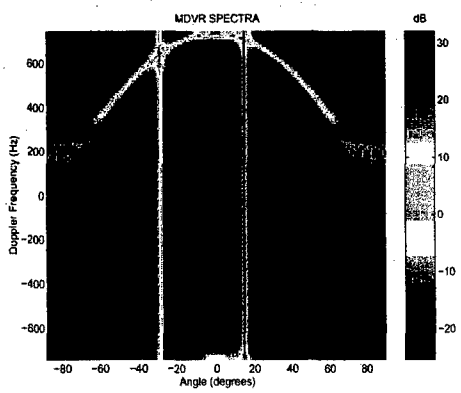

Figure 5. MVDR spectra, medium PRF, forward-looking radar case.

In contrast to the PSD or MVDR spectra, an alternate view of the characteristics arise from an eigen-decomposition. The stochastic space-time snapshot can be written via the Karhunen Loeve transform [7] as

$$\mathbf{x}_k = \sum_{m=1}^{NM} a_m \mathbf{q}_m; \; E[a_m a_m^*] = \lambda_m, \tag{9}$$

where $\mathbf{q}_m$ is an eigenvector of the corresponding covariance matrix with corresponding eigenvalue λ_m. Specifically, from (9),

$$\mathbf{R}_k = \sum_{m=1}^{NM} \lambda_m \mathbf{q}_m \mathbf{q}_m^H. \tag{10}$$

The eigenvector represents a mode of the interference (direction of arrival and Doppler), while the eigenvalue represents the corresponding power. A plot of the rank-ordered eigenvalues is known as the eigenspectrum. The eigenspectrum provides insight into the interference-to-noise ratio and number of DoF the processor requires to cancel the interference. Figure 6 shows the eigenspectra for the side-looking and forward-looking cases yielding the MVDR spectra of Figures 4-5 with the jamming removed. We also include the low pulse repetition frequency (PRF) side-looking case. As a result of Doppler aliasing, the number of eigenvalues above the noise floor increases for the low PRF case; hence, more space-time DoFs are necessary to effectively cancel the interference.

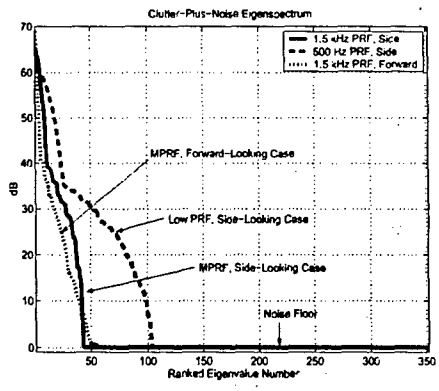

Figure 6. Eigenspectra for side-looking and forward-looking airborne platforms.

We described the SINR loss metric in [1]. Figure 7 shows the estimated SINR loss for the measured data example yielding the result in Figure 3. The legend on each plot indicates the range bin number used to estimate the unknown covariance matrix. The variability among the curves is a consequence of the heterogeneous nature of the clutter environment. For further discussion concerning the impact of heterogeneous clutter on STAP, see [1] and [8].

For comparison, Figure 8 shows a simulated SINR loss plot using the parameters taken from the measured data collection (such as transmit frequency, array size, number of subarrays, navigation data, etc.). We use the model given in (2) to simulate clutter. Observe that the clutter null between measured and simulated data matches perfectly. However, the spectral width of the measured data varies considerably from the simulated case. This occurs because the angle-Doppler relationship is deterministic, yet amplitude and spectral spread is a random process not precisely characterized in the simulation.

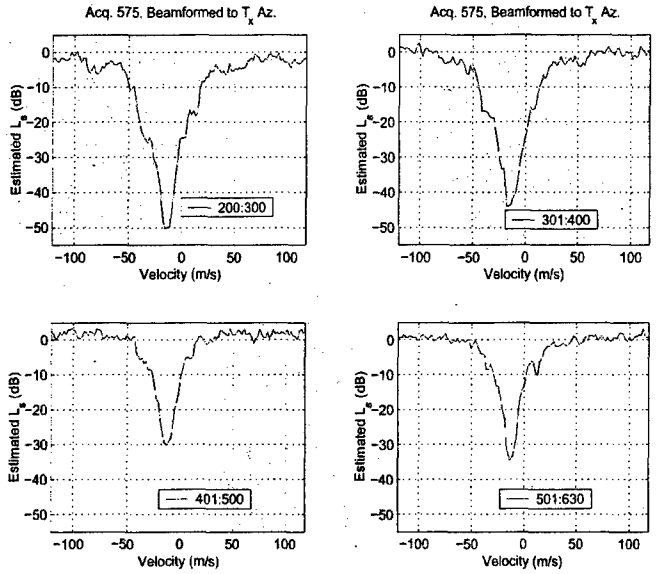

Figure 7. Estimated SINR loss for measured multi-channel airborne radar data.

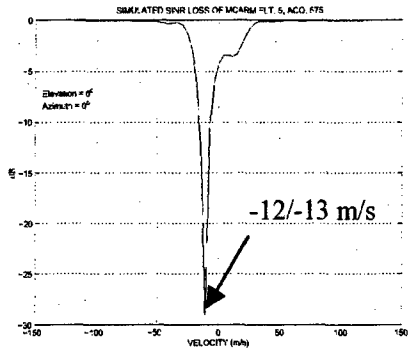

Figure 8. Simulated SINR loss using experimental parameters.

MTI radar operate with three basic PRF designations: low, medium and high. By definition, low PRF radar operate ambiguously in Doppler with no range ambiguity (range fold-over); medium PRF radar are slightly ambiguous in Doppler and range; and, high PRF radar is unambiguous in Doppler and highly ambiguous in range. Generally, high PRF modes are used for AMTI. The range fold-over is a disadvantage, since more clutter competes with the weak target. Also, special processing is necessary to unfold range. Low PRF radar is used in a variety of long range search modes; Doppler aliasing is its main disadvantage. Using STAP, the medium PRF mode is quite attractive. The adaptive processor can null competing sidelobe clutter. Staggering PRFs from dwell-to-dwell, the processor can disambiguate the target Doppler. Figure 9 compares the MVDR spectra for the low, medium and high PRF selections for our side-looking airborne radar example. The Doppler aliasing is notable in the low PRF case; the adaptive processor will used more DoF to cancel the interference in this case. Figure 6 further illustrates the expansion of the interference subspace in the low PRF case through a doubling of the number of significant eigenvalues. The requirement for more DoFs has important ramification when implementing practical reduced-dimension and reduced-rank STAP [1].

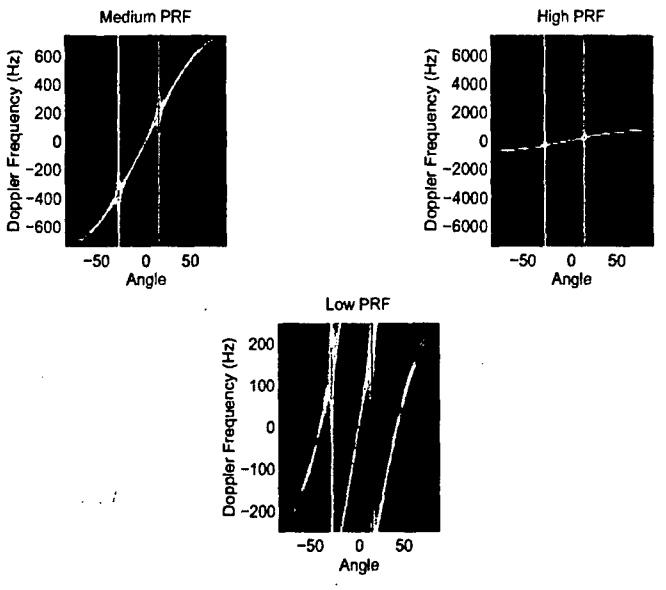

Figure 9. Comparison of MVDR spectra for varying PRF, side-looking airborne radar example.

We conclude this section with a brief discussion of airborne radar training issues. Recall, in [1] we discussed the famous Reed-Mallett-Brennan (RMB) rule [9]: in an iid environment, the STAP requires a secondary (training) data of size twice the total DoF to yield an average output SINR within 3 dB of optimal. Clutter heterogeneity complicates training the STAP processor [1,8]. However, even if the clutter environment were homogeneous, other training challenges exist. The classic configuration for airborne radar STAP analysis is the perfectly side-looking linear array; a perfectly side-looking linear array can experience no yaw or pitch. In this case, clutter Doppler and cone angle are proportional [4]. This implies range invariance among angle-Doppler contours. Hence, assuming a homogeneous clutter environment, the adaptive filter continually converges to the optimal response as the secondary data set size increases. In contrast, in the forward-looking case – the extreme of the side-looking case – angle Doppler contours vary for near in range. As a general rule-of-thumb, if the slant range divided by the platform altitude is less than five, nonstationarity among angle-Doppler contours will exist. Figures 10-11 compare the angle-Doppler contours for side-looking and forward-looking scenarios. All of the contours for varying range align in the side-looking case, but variation for near-in slant range is evident in the forward-looking configuration. Since the STAP must filter in angle and Doppler by using training data chosen over range, any range variation in clutter behavior leads to covariance estimation error and consequent filter mismatch. Hence, SINR and probability of detection decrease accordingly, while the false alarm rate may increase. The variation of angle-Doppler behavior is an especially important consideration in spaceborne and bistatic systems.

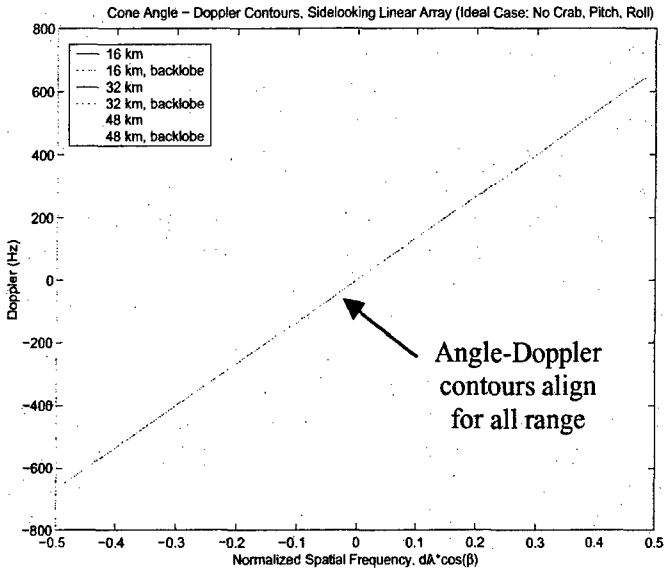

Figure 10. Angle-Doppler contours over range, side-looking airborne radar case.

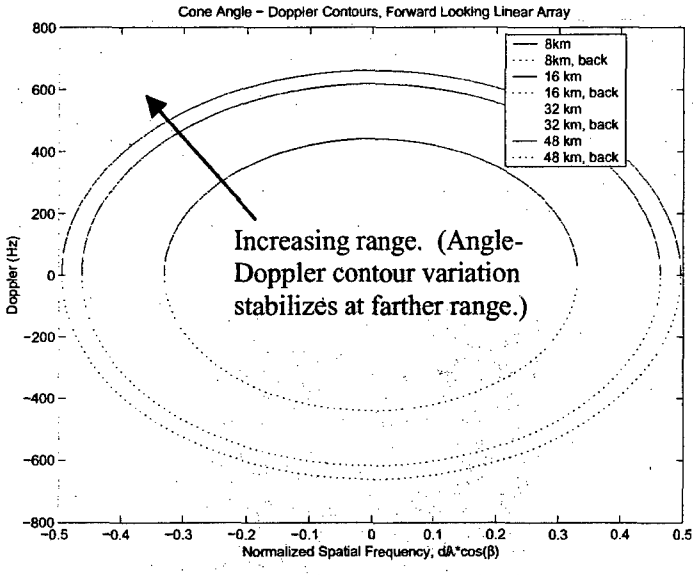

Figure 11. Angle-Doppler contours over range, forward-looking airborne radar case.

3. STAP in Spaceborne Radar

Space-based radar (SBR) provides the potential for continuous surveillance coverage. Since the SBR is down-looking, clutter and jammer mitigation techniques are integral parts of the MTI mode design. In this section we highlight STAP application in GMTI space-based radar. The importance of adequate antenna aperture is a key theme.

Major distinctions between spaceborne and airborne platforms include the very high satellite platform velocity, much steeper operational grazing angles, profound influence of the antenna pattern, the potential for dramatic variation in clutter statistics, size of the antenna footprint on the ground, and the deterministic nature of the satellite orbit. Additionally, the launch vehicle limits the size, power and weight of the SBR system. In low earth orbit, the satellite travels at approximately 7 km/s; this contrasts with the 120-200 m/s velocity of an airborne surveillance radar. At higher grazing angles, the clutter is more specular, thereby increasing the amount of clutter power competing with the target signal. The field of regard for SBR is very large. Hence,

the system can survey large areas, but clutter cultural features can change dramatically. Also, in GMTI SBR, the PRF is set to avoid range ambiguities in the radar footprint. The limited PRF leads to substantial Doppler aliasing. Also, the large footprint increases the number of undesirable emitters in the radar purview. Perhaps, most importantly, the azimuth dimension of the aperture strongly influences mainbeam clutter spread. STAP plays an important role in overcoming some of the diffraction-limited characteristics of deployable space-based arrays whose size is limited by launch vehicle constraints.

We now take a closer look at clutter behavior in SBR. Table 1 provides general simulation parameters, these values are taken from [10]. The effective platform speed incorporates both satellite orbital velocity and the velocity due to the earth's rotation. Effectively using the clutter model of (2), with additional modeling to incorporate orbital mechanics, we arrive at the clutter-plus-noise MVDR spectra of Figure 12. Sixty-four pulses comprise the coherent dwell and the array is linear with twelve spatial channels. Array dimensions are 16 meters in azimuth by 2.5 meters in elevation. The PRF is on the order of 2.2 kHz. The startling observation concerning Figure 12 is the high degree of aliasing, mainly in Doppler, but also in angle. (Angle ambiguity occurs because the separation between the twelve spatial channels far exceeds one-half of a wavelength; the pattern shown in Figure 12 repeats itself in angle.) Figure 12 makes it clear that SBR GMTI is an endo-clutter detection problem: the target signal directly competes with the aliased mainbeam clutter.

Table 1. General Space-Based Radar Analysis Parameters Taken From [10]

Parameter	Value
Array Aperture	40 m^2
Center Frequency	10 GHz
Bandwidth	180 MHz
Clutter Model	-10 dB constant gamma
Platform Altitude	770 km
Grazing Angle	45 degrees
Effective Platform Speed	7.16 km/s

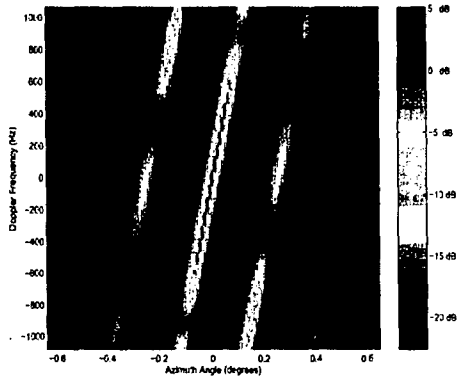

Figure 12. MVDR spectra for SBR example defined in Table 1.

Figure 13 shows the SINR loss curve using the optimal space-time processor (STAP with a clairvoyant covariance matrix) for our example in Table 1. The results provide a good match to those in [10]. Observe the poor performance of the 8 meter azimuth by 5 meter elevation array (40 m^2 total). The shorter azimuth dimension leads to increased beamwidth. The mainbeam clutter spread across this increased beamwidth is very large and due to signal aliasing affects all Doppler frequencies. The 16 meter azimuth by 2.5 meter elevation antenna maintains the required 40 meter-square aperture stow size, yet provides significantly better performance. Since the azimuth beamwidth is much narrower for the 16 meter dimension, mainbeam clutter spread is minimized. The reduced mainbeam clutter spread translates to much better SINR loss performance. Hence, STAP for SBR is a full system design task, coupling algorithm selection with the appropriate selection of radar system parameters.

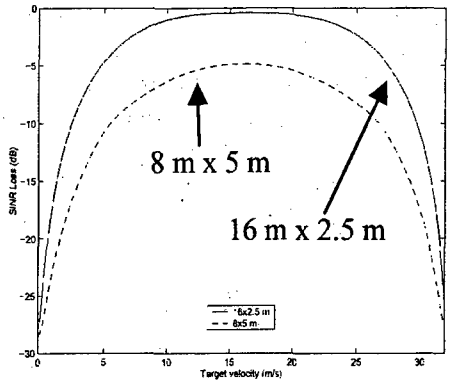

Figure 13. SBR SINR loss for varying antenna size and optimal space-time processing.

A notional signal processing architecture for GMTI is shown in Figure 14 [10]. A multi-channel array is broken into subarrays; the subarrays are then used for adaptive jammer and clutter cancellation. Sub-band filtering is used to compensate for signal bandwidth. Without sub-banding, dispersion across the array degrades cancellation performance. Jammer cancellation occurs in a separate step from clutter mitigation to reduce computational burden and reduce training data requirements. The jammer cancellation step requires a special training interval and operates in beamspace. Jammer canceled beams are then pulse compressed and fed into a beamspace STAP used to mitigate clutter. After clutter cancellation, the processor re-stitches the waveform in the sub-band combiner. Scalar data then proceeds to a detector, such as a cell averaging constant false alarm rate (CA-CFAR) circuit. The post-processor accomplishes target tracking. Adaptive array processing plays a key role in this architecture: a one-dimensional adaptive canceler suppresses the jammer, while the two-dimensional STAP minimizes the impact of clutter on detection performance. Other aspects of the design accommodate unique aspects of adaptive array processing (e.g., sub-banding enables more efficient use of adaptive DoFs). We also point out that by efficiently improving SINR, STAP enables high search rates required for wide area search.

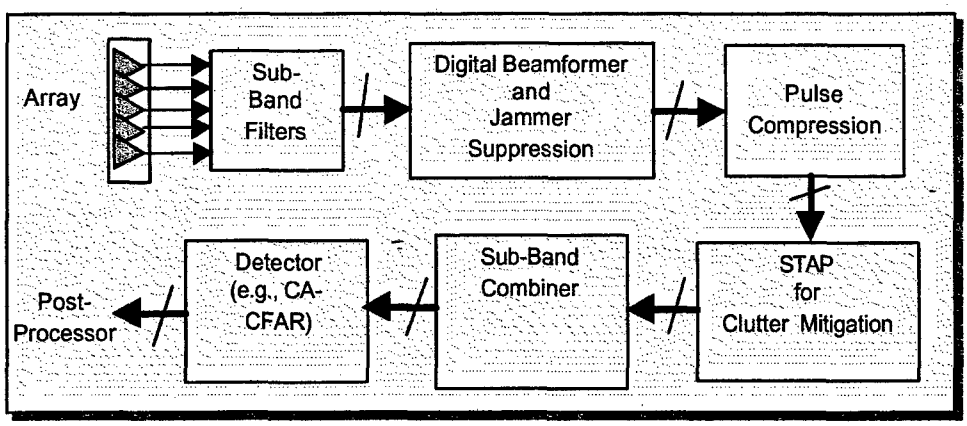

Figure 14. Notional GMTI signal processing chain for space-based radar.

4. Bistatic STAP

Bistatic radar systems use a transmitter and receiver separated by a considerable distance; the distance from transmitter to receiver is usually on the order of the separation from the transmitter to the target. Effective bistatic operation must provide suitable means for mitigating bistatic clutter. Figure 15 provides an overview of the origins of bistatic clutter. Four possible paths, identified in the figure, give rise to the clutter signal. Additionally, the two-way gain to points on the iso-range (an ellipse in bistatic radar) tends to be fairly high,

resulting in strong, spectrally diverse clutter. In light of Figure 15, adaptive clutter nulling appears to be an essential system component. Thus, extending STAP techniques developed for monostatic systems is a logical step in combating bistatic clutter. Bistatic STAP techniques are considered in [11-14].

In this section we highlight some key aspects of bistatic STAP. Specifically, bistatic clutter is nonstationary. Nonstationarity leads to covariance estimation errors and hence degrades adaptive filter performance. After considering the deleterious effect of nonstationarity, we investigate several ameliorating techniques, including localized STAP processing and time-varying weight methods.

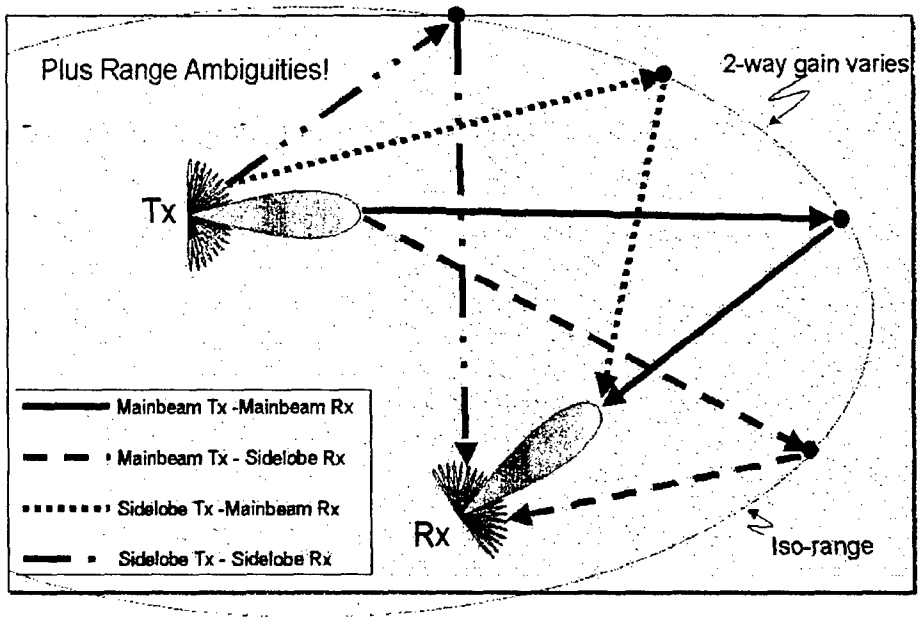

Figure 15. Overview of bistatic system and origin of diverse clutter.

Recall, when implementing the adaptive filter it is common to use the sample covariance estimate

$$\hat{\mathbf{R}}_k = \frac{1}{L}\sum_{\substack{m=1 \\ m\neq k}}^{L} \mathbf{x}_m \mathbf{x}_m^H \tag{11}$$

which is maximum likelihood when the data are jointly Gaussian and iid [9]. When the training data are iid, approximately $2NM$ vector samples are necessary in (11) to attain an average SINR loss of 3 dB between adaptive and optimal filters.

As a consequence of the iid assumption, $E\left[\hat{\mathbf{R}}_k\right] = \mathbf{R}_k$. Thus, in the iid case the adaptive filter asymptotically approaches the performance of the optimal filter. Typical bistatic radar environments deviate from iid conditions; under such circumstances, $\mathbf{R}_k \neq \mathbf{R}_m$ over many range realizations, m, and so the estimate of (11) does not asymptotically approach $\mathbf{R}_k$, but rather tends to an "average" response related to the variable properties of the training data. Bistatic geometry leads to range-varying clutter behavior (i.e., $\mathbf{R}_k \neq \mathbf{R}_m$).

Bistatic geometry is the source of clutter nonstationarity. Associate a right-handed coordinate system with both the transmitter and receiver. In each case, the x-axis points North, the y-axis points West and the z-axis points upwards. In general, a unit vector pointing from a given platform to a stationary point on the ground is

$$\mathbf{k}(\phi,\theta) = \cos\theta\sin\phi\hat{\mathbf{x}} + \cos\theta\cos\phi\hat{\mathbf{y}} + \sin\theta\hat{\mathbf{z}}, \tag{12}$$

where ϕ is azimuth measured positive in the clockwise direction from the y-axis and θ is elevation measured negative in the downward direction from the horizon. With these definitions, the bistatic Doppler of a given clutter patch is

$$f_{bistatic} = \frac{1}{\lambda}\left[\mathbf{k}_{\mathbf{Tx}}(\phi_{Tx},\theta_{Tx})\cdot\mathbf{v}_{\mathbf{Tx}} + \mathbf{k}_{\mathbf{Rx}}(\phi_{Rx},\theta_{Rx})\cdot\mathbf{v}_{\mathbf{Rx}}\right]. \tag{13}$$

The subscripts *Tx* and *Rx* denote transmitter and receiver quantities, respectively. Also, $\mathbf{v}_{\mathbf{Tx}}$ and $\mathbf{v}_{\mathbf{Rx}}$ are transmit and receive platform velocity vectors, respectively. Both transmitter and receiver contribute to the Doppler of the clutter patch. The spatial phase among receiver channels due to bistatic scattering from a stationary point varies with array mounting and scatterer location. Bistatic clutter angle-Doppler properties vary in a complex manner with the particular geometry. Numerical simulation is the best recourse for computing the varying angle-Doppler behavior with bistatic range sum. An example of angle-Doppler characteristics in the bistatic case is given in Figure 16; the variation of the clutter loci over range leads to filter mismatch and the potential for poor instantaneous performance.

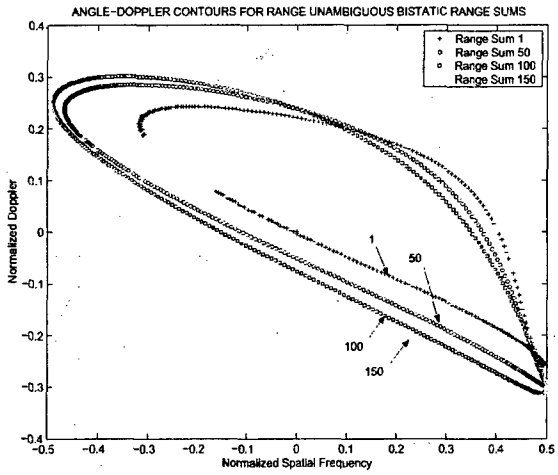

Figure 16. Angle-Doppler contours for varying bistatic range sum.

To further evaluate the impact of bistatic geometry on STAP, we consider an example bistatic configuration designed to extend the noise-limited performance of the transmit platform. The receiver is at an altitude of 4 km. With respect to the receiver, the transmitter is at 93 degrees elevation from nadir and 92 degrees azimuth from true-North. The transmit antenna boresight points 270 degrees in azimuth from true-North, while the receive antenna normal points to 268 degrees. The bistatic baseline is 100 km and the transmitter and receiver are in level flight, with the transmit velocity vector remaining at 100 m/s in the x-direction and the receiver velocity vector being 12 m/s in the x-direction and 97 m/s in the y-direction.

Figures 17 and 18 show the clairvoyant SINR loss ($L_{s,1}$, see [1]) and SINR loss due to adaptivity ($L_{s,2}$, see [1]). Nonstationarity is evident in Figure 17 since the contour curves through the range-Doppler map. The consequences of varying bistatic clutter behavior are seen in Figure 18: SINR losses are fairly substantial. In this latter case, the whole set of space-time snapshots are used for training and so we expect Figure 18 to represent a worst case scenario.

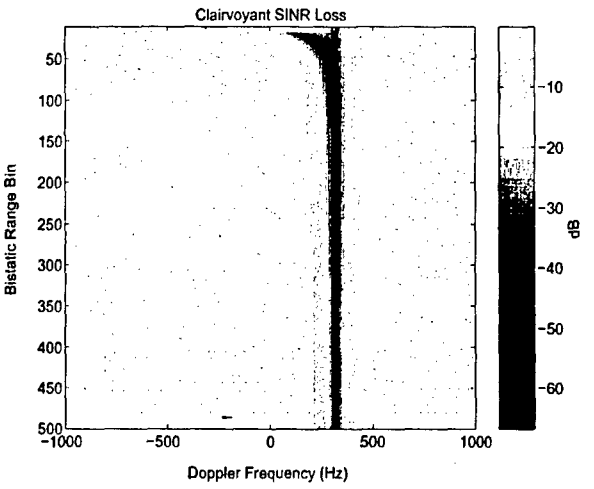

Figure 17. Clairvoyant SINR loss for example bistatic configuration.

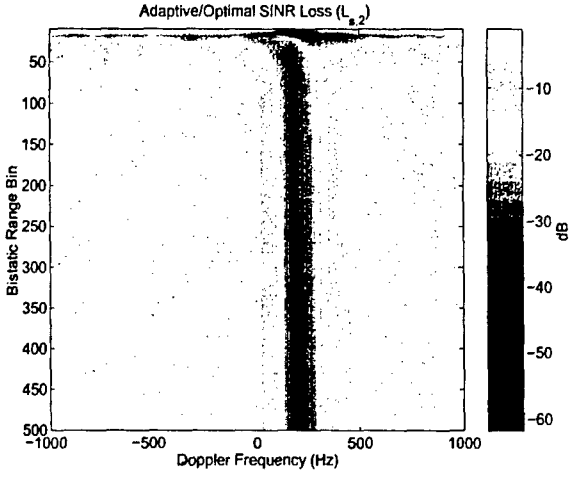

Figure 18. SINR loss between adaptive and optimal filters for example bistatic configuration.

Three approaches to enhance STAP performance, present in the available literature, include: localized STAP [12-14], time-varying weights [11,12,14], and angle-Doppler contour warping [11]. In the first approach, an appropriate reduced-dimension or reduced-rank STAP technique is used to minimize the training data set; minimal variation of bistatic angle-Doppler contours over the reduced training regions serves as the underlying assumption of this approach. A time-varying weight technique was first described in [15] for jammer cancellation in moving arrays and later extended to the bistatic STAP problem. The basic idea involves expanding the adaptive weight vector via a Taylor series over range r, discretizing and truncating the series to first order, and then forming the time-varying filter, viz.

$$\mathbf{w}(r) = \mathbf{w}\big|_{r=0} + r\,\dot{\mathbf{w}}\big|_{r=0} + \frac{r^2}{2}\,\ddot{\mathbf{w}}\Big|_{r=0} + \cdots;$$

$$\mathbf{w}_k = \mathbf{w}_0 + k\Delta\mathbf{w};\quad y_k = \underbrace{\left[\mathbf{w}_0^{\mathbf{H}} \quad \Delta\mathbf{w}^{\mathbf{H}}\right]}_{\mathbf{z}}\begin{bmatrix}\mathbf{x}_k \\ k\mathbf{x}_k\end{bmatrix}; \tag{14}$$

$$\mathbf{z} = \frac{\mathbf{R}_{ext}^{-1}\mathbf{s}_{st,ext}}{\mathbf{s}_{st,ext}^{\mathbf{H}}\mathbf{R}_{ext}^{-1}\mathbf{s}_{st,ext}},$$

where $\mathbf{R}_{ext}$ is the covariance matrix of the extended data vector $[\mathbf{x}_k^T \quad k\mathbf{x}_k^T]^T$ and $\mathbf{s}_{s\text{-}t,ext}$ is the extended weight vector. From (14) we note the following: the dimensionality is doubled to accommodate a time-varying response, but required training data also doubles and computation load can increases substantially if the processor applies frequent updates (which the time-varying behavior may obviate). In the Doppler warping technique [11], the processor uses *a priori* knowledge to align angle-Doppler contours over range at specific points. We briefly consider the former two approaches.

Figure 19 shows the SINR loss for various reduced-dimension (RD) STAP methods applied to our bistatic example for bistatic ranges 25 and 150, along with the upper bound given by the clairvoyant joint domain optimum (JDO) implementation. JDL_{3x3} and JDL_{5x5} represent the Joint Domain Localized (JDL) method given in [16]; the subscript refers to the number of spatial beams and Doppler filters used to define the localized processing region. JDL adaptively combines select beams and Doppler filters, thereby managing both spatial and temporal DoFs. The minimum training size for JDL_{3x3} is 18 range bins, while 50 range bins define the minimum size for JDL_{5x5}. EFA_{3temp} signifies the Extended Factored Algorithm [17] with three temporal degrees of freedom. EFA uses all spatial DoFs and a subset (three in this case) of the temporal DoFs; the minimum training size is 66 bistatic range bins. Adaptive Displaced Phase Center Antenna (ADPCA) processing uses a covariance matrix to whiten the clutter and a steering vector resembling a pulse-to-pulse canceler to further suppress interference [18]. $ADPCA_{2temp}$ uses all spatial channels and two temporal DoFs in its implementation; 44 range bins is the minimum sample size for covariance estimation.

Figure 19 indicates that all RD-STAP methods significantly improve performance over the joint space-time approach. JDL_{5x5} exhibits the best capability for both ranges of interest, while $ADPCA_{2temp}$ performs the worst (pre-steering the ADPCA temporal steering vector to the center of the clutter spectra is a challenge in both instances). The performance of EFA_{3temp} and JDL_{3x3} varies: JDL_{3x3} outperforms EFA_{3temp} for the near range, while the opposite is true for range bin 150. This figure suggests the complexity in allocating spatial and temporal DoFs versus minimizing the required sample support. JDL_{5x5} appears to represent the best trade in this regard.

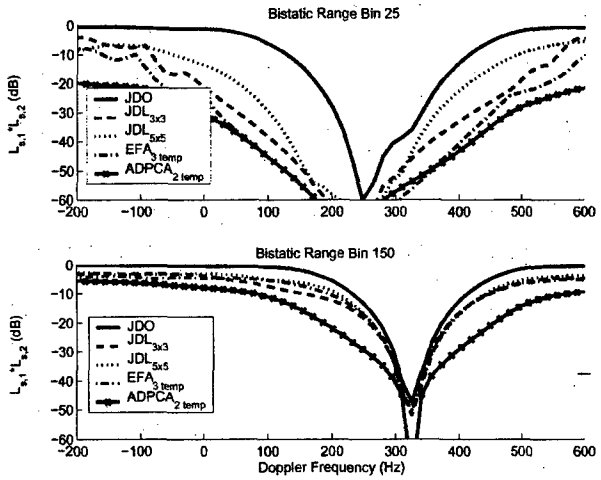

Figure 19. Comparison of reduced-dimension STAP performance applied to example bistatic configuration.

Incorporating the time-varying weight approach of [15] with JDL affords the potential to exploit localized processing while tracking clutter nonstationarity. As previously mentioned, the time-varying weight method effectively doubles the processor's DoFs, and so the minimum training set size also doubles. Figure 20 shows the successful application of the time-varying method of Hayward to JDL for bistatic STAP. The minimum detectable velocity (MDV) of the radar is significantly enhanced when using the time-varying weight procedure. Overall performance gains range from 5 dB to 10 dB, depending on Doppler frequency and JDL implementation (3x3 or 5x5).

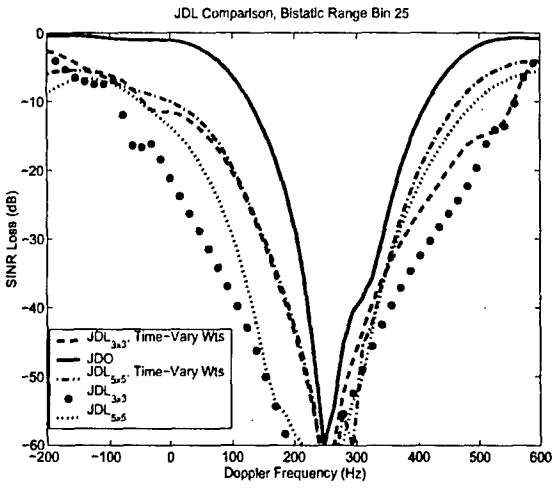

Figure 20. Application of time-varying weight procedure to example bistatic configuration.

5. Terrain Scattered Jamming Suppression

Our prior examples involve using spatial and slow-time degrees of freedom to mitigate ground clutter and narrowband jamming. In this previous discussion, we assume the jamming is a direct path signal. Terrain scattered jamming (TSJ) occurs when the radar aperture captures jamming energy reflecting off the earth's surface. Note, terrain scattered jamming may or may not be intentional. Commonly, a direct path jamming signal is present and the TSJ enters the antenna mainbeam. Spatial and slow-time degrees of freedom are not applicable in this instance. Rather, the processor must make use of spatial and fast-time taps to suppress the TSJ signal. An excellent overview of TSJ is available in [19]. Synonyms for terrain scattered jamming include jammer multipath and hot clutter. The approach to TSJ suppression has analogous application in communication systems.

We briefly highlight some aspects of TSJ mitigation for a ground-based radar example. The geometry of interest is shown in Figure 21. The direct path jamming prevents the radar from determining the range to the target (jammer). Burn-through is a costly option, affecting the radar time-line. In this case, unintentional jamming reflects off the earth's surface. The specular point occurs where the angle of incidence, a_i, roughly equals the angle of reflection a_r. A region of diffuse scattering is known as the glistening surface; its extent relates to the roughness of the terrain in a root mean square (RMS) sense. Since the jammer enters the antenna mainbeam, applying a spatial null cancels not only the jammer, but the target signal as well.

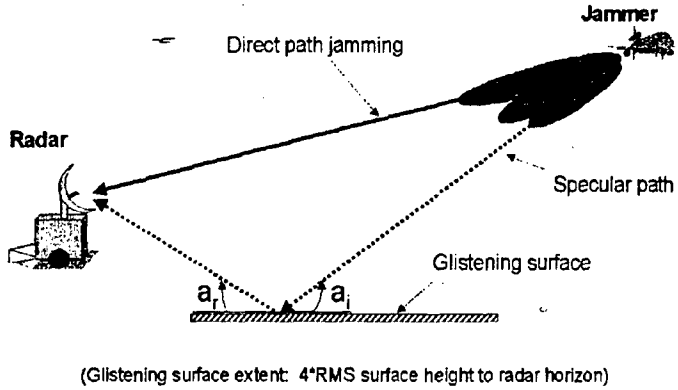

Figure 21. TSJ geometry for ground-based radar example.

The jammer space and fast-time snapshot is given by

$$\bar{\mathbf{x}}_{\mathbf{k}}(l) = \sum_{m=0}^{q} \alpha_m \, \mathbf{s}_{\mathbf{s}}(\phi_m, \theta_m) e^{-j2\pi f_{d/m}(lT_p + k\tau)} w(lT_p + k\tau - D_m) \tag{15}$$

where α_m is the amplitude factor of the mth signal term and is proportional to the reflection coefficient and square root of the jammer power, $\mathbf{s}_{\mathbf{s}}(\theta_m, \phi_m) \in C^{Mx1}$ represents the direct or TSJ (multipath) spatial steering vector measured over the M spatial channels, θ_m is elevation angle, ϕ_m is azimuth angle, $f_{d/m}$ is the Doppler offset due to the jammer motion, $w(t)$ is the complex jammer waveform, and D_m is the path length delay for the mth signal with respect to the direct path. Also, T_p is the pulse repetition interval and τ is the fast-time sampling rate (generally, τ is the reciprocal of the receiver bandwidth). Fast and slow-time indices are given by k and l, respectively. It is important to note from (15) that each TSJ component is a scaled, time-delayed version of the direct path jamming.

The application of STAP to TSJ mitigation is best understood by considering the generalized sidelobe canceler (GSC) STAP architecture [7]. The GSC is shown in Figure 22. The space and fast-time steering vector is $s_{s-fi}(\phi, \theta, k)$, $\mathbf{B}$ is a blocking matrix preventing the desired signal from entering the lower leg of the filter, d_o is the quiescent response, $\mathbf{w}_{\mathbf{GSC/k}}$ is the weight vector chosen to minimize the mean square error ε_o between d_o and its estimate $\hat{d}_o = \mathbf{w}_{\mathbf{GSC/k}}^H \bar{\mathbf{x}}_{\mathbf{k/0}}$. The weight vector follows from the Wiener-Hopf equations [7], taking the form

$$\mathbf{w}_{\mathbf{GSC/k}} = \mathbf{R}_{\bar{\mathbf{x}}_{\mathbf{k/0}}}^{-1} \mathbf{r}_{\mathbf{d_o}, \bar{\mathbf{x}}_{\mathbf{k/0}}}; \; \mathbf{R}_{\bar{\mathbf{x}}_{\mathbf{k/0}}} = \mathrm{E}\left[\bar{\mathbf{x}}_{\mathbf{k/0}} \bar{\mathbf{x}}_{\mathbf{k/0}}^H\right]; \; \mathbf{r}_{\mathbf{d_o}, \bar{\mathbf{x}}_{\mathbf{k/0}}} = E\left[d_o^* \bar{\mathbf{x}}_{\mathbf{k/0}}\right]. \tag{16}$$

Thus, in the top leg, the GSC forms a quiescent beam in the target (jammer) direction, blocks the desired signal in the bottom leg, and then attempts to estimate the TSJ in the top leg using correlated information in the bottom leg to minimize the mean square error output. Effectively, the GSC scales and time-delays the TSJ in the bottom leg to cancel the the TSJ competing with the desired signal in the top leg. The target signal will appear as residue in ε_o. If the residue is substantial, it will cross the detection threshold and the processor will declare target presence. Interestingly, the TSJ provides a source for overcoming the direct path, mainbeam jamming!

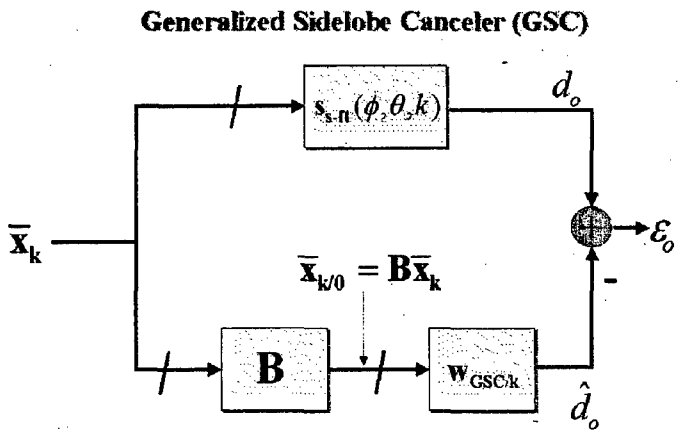

Figure 22. Generalized sidelobe canceler architecture for space and fast-time adaptive cancellation.

We may specify $w(t)$ stochastically by choosing an appropriate power spectral density or autocorrelation model. Such models for the jammer autocorrelation function, $\Phi(\tau)$, typically include

$$\Phi(\tau) = \begin{cases} \sin c(\pi \cdot BW \cdot \tau) \\ \exp(-BW^2 \cdot \tau^2); \quad BW = \min(BW_{Rx}, BW_{Jammer}), \\ \delta(\tau) \end{cases} \tag{17}$$

where BW_{Rx} and BW_{Jammer} signify receiver (Rx) and jammer bandwidth. The delta function model is unrealistic. Figure 23 depicts the autocorrelation function for the former cases. The choice of model will impact the effectiveness of the STAP [20].

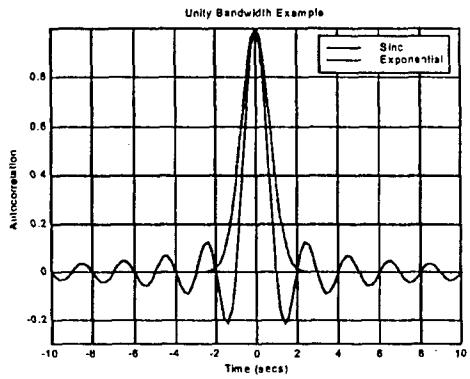

Figure 23. Potential autocorrelation functions for the jammer waveform.

Figures 24 and 25 correspond to the scenario of a mainbeam escort jammer masking the detection of the desired target. Figure 24 indicates that effective STAP performance relies on adequate terrain bounce energy; a strong signal is needed for the adaptation. Figure 25 compares the filter output for a non-adaptive beamformer and the STAP architecture of Figure 23. The target signal is marked in the figure and is clearly visible for the STAP case, whilst buried in the noise for the non-adaptive beamforming method.

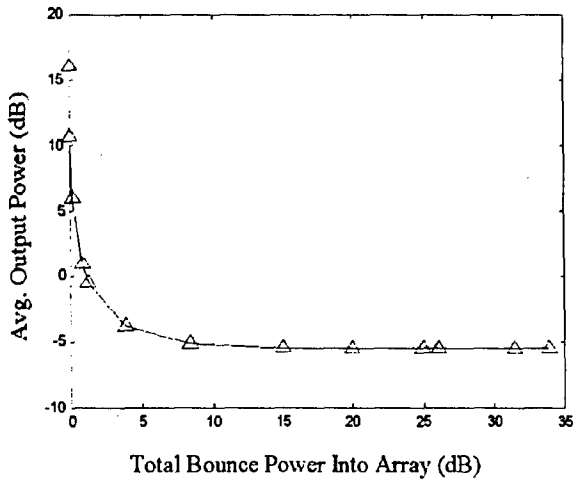

Figure 24. Effective processing relies on adequate multipath signal.

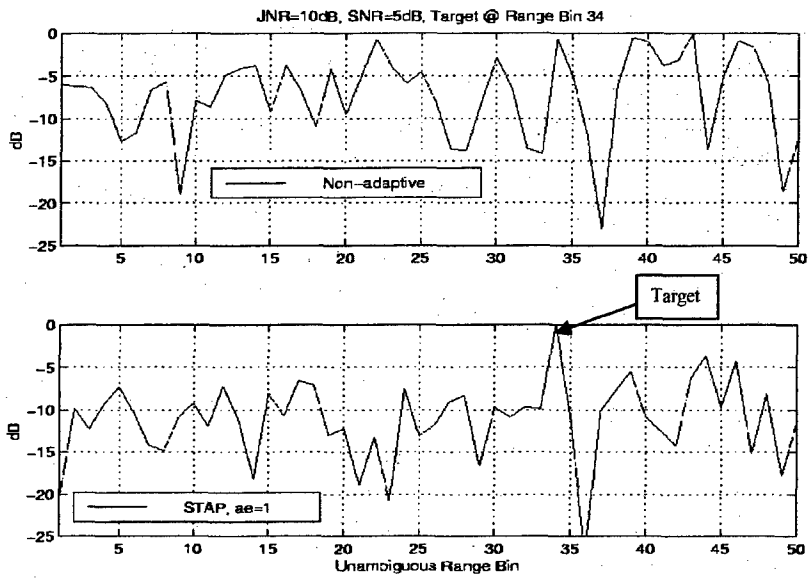

Figure 25. Comparison of non-adaptive beamformer and STAP.

6. Summary

In this set of lecture notes we apply the basic STAP theory developed in [1] to several practical applications. We begin by considering STAP in airborne radar systems. Topics covered include development of basic space-time models for ground clutter and noise jamming, clutter and jamming power spectral densities and minimum variance spectra, the impact of pulse repetition frequency on clutter characteristics, comparison of simulated and actual measured data, and some training-related issues. Next, we build on the airborne STAP discussion by describing STAP's role in ground moving target indication from spaceborne platforms. The key theme in our discussion is the importance of aperture on overall detection performance and application of STAP to overcome diffraction-limited performance bounds. We then describe airborne bistatic STAP. Bistatic clutter environments are nonstationary. Nonstationarity affects STAP implementation by corrupting the covariance estimation procedure. We consider localized STAP and a time-varying weight procedure to enhance bistatic STAP performance. Finally, we overview adaptive space and fast-time processing for terrain scattered and mainbeam jammer suppression. In this case, the terrain scattered jamming appears as scaled, time-delayed replicas of the mainbeam jamming signal. Using the generalized sidelobe canceler architecture, we investigate the manner in which STAP suppresses both mainbeam and terrain scattered jamming signals to enable target detection.

References

[1] W.L. Melvin, "Space-time detection theory," *Proceedings of the Research and Technology Agency, North Atlantic Treaty Organization (RTA-NATO) Lecture Series 228 – Military Applications of Space-Time Adaptive Processing*, September 2002.

[2] I.S. Reed, "A brief history of adaptive arrays," Sudbury/Wayland Lecture Series (Raytheon Div. Education) Notes, 23 October 1985.

[3] L.E. Brennan and I.S. Reed, "Theory of adaptive radar," *IEEE Trans. AES*, Vol. 9, No. 2, March 1973, pp. 237-252.

[4] R. Klemm, Space-Time Adaptive Processing: Principles and Applications, IEE Radar, Sonar, Navigation and Avionics 9, IEE Press, 1998.

[5] J. Ward, *Space-Time Adaptive Processing for Airborne Radar*, Lincoln Laboratory Tech. Rept., ESC-TR-94-109, December 1994.

[6] D.K. Fenner and W.F. Hoover, "Test results of a space-time adaptive processing system for airborne early warning radar," *Proc. 1996 IEEE Natl. Radar Conf.*, Ann Arbor, MI, 13-16 May 1996, pp. 88-93.
[7] S. Haykin, Adaptive Filter Theory, Third Ed., Prentice-Hall, Upper Saddle River, NJ, 1996.
[8] W.L. Melvin, "Space-time adaptive radar performance in heterogeneous clutter," *IEEE Trans. AES*, Vol. 36, No. 2, April 2000, pp. 621-633.
[9] I.S. Reed, J.D. Mallett, and L.E. Brennan, "Rapid convergence rate in adaptive arrays," *IEEE Trans. AES*, Vol. 10, No. 6, November 1974, pp. 853-863.
[10] D. Rabideau and S. Kogon, "A signal processing architecture for space-based GMTI radar," *Proc. 1999 IEEE Radar Conference*, Waltham, MA, pp. 96-101.
[11] S.M. Kogon and M.A. Zatman, "Bistatic STAP for airborne radar systems," *Proc. IEEE SAM 2000*, Lexington, MA, March 2000.
[12] W.L. Melvin, M.J. Callahan and M.C. Wicks, "Adaptive clutter cancellation in bistatic radar," *Proc. 34th Asilomar Conf.*, Pacific Grove, CA, 29-31 Oct 00, pp. 1125-1130.
[13] B. Himed, J.H. Michels and Y. Zhang, "Bistatic STAP performance analysis in radar applications," *Proc. 2001 IEEE Radar Conf.*, Atlanta, GA, May 2001, pp. 198-203.
[14] W.L. Melvin, M.J. Callahan and M.C. Wicks, "Bistatic STAP: application to airborne radar," to appear in *Proc. 2002 IEEE Radar Conference*, Long Beach, CA, 22-25 April 2002.
[15] S.D. Hayward, "Adaptive beamforming for rapidly moving arrays," *Proc. CIE Int'l Conf of Radar* (IEEE Press), Beijing, China, October 1996, pp. 480-483.
[16] H. Wang and L. Cai, "On adaptive spatial-temporal processing for airborne surveillance radar systems," *IEEE Trans. AES*, Vol. 30, No. 3, July 1994, pp. 660-670.
[17] R.C. DiPietro, "Extended factored space-time processing for airborne radar," *Proc. 26th Asilomar Conf.*, Pacific Grove, CA, Oct. 1992, pp. 425-430.
[18] R. Blum, W. Melvin and M. Wicks, "An analysis of adaptive DPCA," *Proceedings of the 1996 IEEE National Radar Conference*, Ann Arbor, Michigan, May 13-16, 1996, pps. 303-308.
[19] P. Techau, J. Guerci, T. Slocumb, L. Griffiths, "Performance bounds for hot and cold clutter mitigation," *IEEE Trans. AES*, Vol. 35, No. 4, October 1999, pp. 1253-1265.
[20] P.M. Techau, "Effects of receiver filtering on hot clutter mitigation," *Proc. 1999 IEEE Radar Conf.*, Waltham, MA, 20-22 April 1999, pps. 84-89.